Journal of
Ceramic Science
and Technology

*J. Ceram. Sci. Technol.*, **17** [3] 201-212 (2026)
DOI: 10.4416/JCST2026-00002
available online at: http://www.ceramic-science.com
© 2026 Göller Verlag

# Zirconia-Toughened Alumina Insert Washers for Suspension Components: Coupled Tribocorrosion-Erosion Behavior in Road-Splash Media

**Zhi Yang***

College of Vehicle Engineering, Chongqing Industry Polytechnic University, Chongqing, 401120, China
received February 14, 2026; received in revised form April 27, 2026; accepted May 24, 2026

**Abstract**

**Zirconia-toughened alumina composites with zirconia contents of 10, 20, and 30 vol% were systematically investigated as candidate insert washer materials for suspension components operating in aggressive road-splash environments. Nearly fully dense ceramics (> 99.5 %) were fabricated by means of pressureless sintering at 1 550 °C, exhibiting a progressive trade-off between hardness and fracture toughness. The incorporation of zirconia increased fracture toughness from 3.6 MPa·m$^{1/2}$ for monolithic alumina to a maximum of 8.1 MPa·m$^{1/2}$ at 20 vol% zirconia, while hardness decreased from 18.2 to 17.1 GPa. Tribocorrosion-erosion behavior was evaluated using a slurry jet impingement system with a simulated road-splash medium consisting of 3.5 wt% NaCl and 200 – 300 µm silica particles at a velocity of 10 m s$^{-1}$ and an impingement angle of 45°. After 24 h exposure, monolithic alumina exhibited severe degradation with a cumulative volume loss of 0.86 mm³, whereas the optimized composite with 20 vol% zirconia showed the lowest loss of 0.15 mm³, corresponding to a steady-state erosion rate of 5.9 × 10$^{-3}$ mm³ h$^{-1}$. Electrochemical measurements revealed that mechanical damage significantly increased surface electrochemical activity for all ceramics; however, zirconia-toughened alumina maintained lower post-test corrosion current densities compared with monolithic counterparts. Post-mortem analyses demonstrated that brittle grain pull-out dominated degradation in alumina, while crack arrest and deflection associated with stress-induced tetragonal-to-monoclinic zirconia transformation governed material removal in the composites. These results identify an optimal balance of hardness and toughness that minimizes coupled mechanical and electrochemical degradation under realistic slurry impingement conditions.**

*Keywords: Transformation toughening, slurry jet impingement, phase stability, erosion resistance, electrochemical response*

## I. Introduction

The relentless pursuit of enhanced vehicle performance, longevity, and safety has catalyzed significant advancements in automotive materials science. Suspension systems, in particular, are critical assemblies that govern vehicle dynamics, ride comfort, and stability [1]. These systems operate in one of the most punishing environments experienced by any automotive component, being constantly subjected to dynamic loads, vibrations, and aggressive environmental attacks [2]. A pervasive and highly detrimental environmental factor is road splash, a complex mixture of water, abrasive particles such as sand and road debris, and corrosive agents, most notably de-icing salts like sodium chloride (NaCl) and calcium chloride used in colder climates [3]. This medium gives rise to a complex and synergistic degradation phenomenon known as tribocorrosion-erosion, where mechanical wear from impacting and sliding particles is accelerated by electrochemical corrosion, and vice versa [4]. The mechanical action continually removes passive or protective surface layers, exposing fresh material to the corrosive electrolyte, while corrosion can weaken the material surface, making it more susceptible to mechanical removal [5].

Traditionally, suspension components such as washers, bushings, and joints have been fabricated from metals and their alloys, or more recently, from engineering polymers [6]. While cost-effective, metallic components are highly susceptible to corrosion, particularly galvanic corrosion and crevice corrosion, when exposed to saline road splash [7]. Protective coatings can mitigate this but are prone to being breached by erosive particle impacts, leading to localized catastrophic corrosion [8]. Engineering polymers, while offering excellent corrosion resistance, often lack the requisite mechanical stiffness, creep resistance, and dimensional stability, especially under the wide temperature fluctuations experienced in automotive applications [9]. This creates a compelling need for a new class of materials that can provide superior resistance to the coupled chemical and mechanical degradation mechanisms inherent to the suspension environment [10].

Advanced engineering ceramics have emerged as strong candidates for such demanding applications

* Corresponding author: 360680758@163.com)

due to their exceptional hardness, high compressive strength, chemical inertness, and thermal stability [11]. Among monolithic ceramics, alumina ($Al_2O_3$) is valued for its extreme hardness and wear resistance, while zirconia ($ZrO_2$) is renowned for its exceptional fracture toughness, a property not typically associated with ceramics [12]. However, monolithic alumina suffers from inherent brittleness, making it prone to catastrophic failure from impact damage, while monolithic zirconia has lower hardness and stiffness compared to alumina [13]. To overcome these individual limitations, Zirconia-Toughened Alumina (ZTA) composites have been developed. These materials ingeniously combine the superior hardness and stiffness of an alumina matrix with the toughening effect of dispersed zirconia particles [14]. The primary toughening mechanism in ZTA is stress-induced phase transformation, where metastable tetragonal zirconia (t-$ZrO_2$) particles transform into the more stable monoclinic phase (m-$ZrO_2$) in the high-stress field ahead of a propagating crack [15]. This transformation is accompanied by a volume increase of approximately 3 – 5 %, which generates compressive stresses that oppose crack opening, thereby significantly enhancing the material's fracture toughness [16]. This unique combination of properties makes ZTA an outstanding candidate for wear- and impact-resistant components like the insert washers in suspension assemblies [17].

Despite the theoretical promise of ZTA for such applications, a significant gap exists in the scientific literature regarding its performance under realistic, simulated road-splash conditions. While numerous studies have investigated the wear resistance [18] or corrosion behavior [19] of ZTA in isolation, very few have explored the coupled tribocorrosion-erosion phenomena that dominate in this specific automotive context. The synergistic interactions between mechanical particle impingement and saline corrosion are poorly understood for this class of advanced ceramics. Consequently, there is a critical need for a systematic investigation to characterize the performance of ZTA and elucidate the underlying degradation mechanisms when it is subjected to a simulated road-splash environment.

This research aims to address this knowledge gap by conducting a comprehensive study on the tribocorrosion-erosion behavior of ZTA insert washers. The primary objectives are: (1) to synthesize and characterize high-density ZTA composites with systematically varied zirconia content (10, 20, and 30 vol%); (2) to perform controlled tribocorrosion-erosion tests using a custom-developed slurry jet impingement system with a simulated road-splash medium containing silica abrasives and a 3.5 % NaCl solution; (3) to benchmark the performance of the ZTA composites against monolithic alumina and yttria-stabilized zirconia (YSZ); and (4) to conduct extensive post-mortem analysis using advanced characterization techniques to identify the dominant degradation mechanisms, with a particular focus on the role of the stress-induced phase transformation. The findings from this work are expected to provide crucial performance data and mechanistic insights, paving the way for the confident design and implementation of durable advanced ceramic components in next-generation automotive suspension systems.

## II. Materials and Methods

### *(1) Materials synthesis and sample preparation*

Five distinct ceramic compositions were prepared for this study to enable a comparative analysis. The baseline materials were a monolithic alumina (designated A100) and a monolithic 3 mol% yttria-stabilized zirconia (3Y-TZP, designated Z100). The composite materials consisted of Zirconia-Toughened Alumina with 10, 20, and 30 volume percent of 3Y-TZP, designated ZTA10, ZTA20, and ZTA30, respectively. The starting powders were a high-purity (99.99 %) $\alpha$-$Al_2O_3$ powder (average particle size 0.4 μm) and a 3Y-TZP powder (average particle size 0.2 μm).

For each ZTA composition, the requisite amounts of $Al_2O_3$ and 3Y-TZP powders were weighed and mixed by means of wet ball milling for 24 hours in an ethanol medium using zirconia grinding balls to ensure homogeneous distribution [14]. Following milling, the slurries were dried in an oven at 80 °C for 48 hours, and the resulting dried cakes were gently crushed and sieved through a 200-mesh screen to break up soft agglomerates. The monolithic A100 and Z100 powders were processed similarly to ensure a consistent processing history. The powders were then uniaxially pressed into discs of 25 mm diameter and 5 mm thickness, followed by cold isostatic pressing (CIP) at 200 MPa to achieve high green density and uniformity. Sintering was performed in a high-temperature furnace in an air atmosphere. The samples were heated at a rate of 5 K/min to a peak temperature of 1 550 °C and held for 2 hours to facilitate full densification, a temperature known to promote good mechanical properties in ZTA systems [20]. The furnace was then cooled at a rate of 10 K/min. After sintering, the flat faces of the ceramic discs were ground and polished to a mirror finish with a final 1 μm diamond suspension for subsequent characterization and testing.

### *(2) Pre-test material characterization*

The bulk density and apparent porosity of the sintered samples were determined using the Archimedes method in distilled water, following ASTM C373 standards. The phase composition of each material was analyzed by means of X-ray Diffraction (XRD) using a diffractometer with Cu $K_\alpha$ radiation ($\lambda$ = 1.5406 Å). Scans were performed over a 2$\theta$ range of 20° to 80° with a step size of 0.02°. The quantitative phase analysis, including the volume fractions of $\alpha$-$Al_2O_3$, tetragonal $ZrO_2$ (t-$ZrO_2$), and monoclinic $ZrO_2$ (m-$ZrO_2$), was carried out using the Rietveld refinement method. The microstructure of the sintered ceramics was examined using a Field Emission Scanning Electron Microscope (FE-SEM). For this, polished samples were thermally etched at 1 450 °C for 20 minutes to reveal the grain boundaries. The distribution of alumina and zirconia phases was observed in backscattered electron (BSE) mode, where the higher atomic number zirconia phase appears brighter

than the alumina matrix [21]. The average grain sizes of the alumina and zirconia phases were determined from the SEM micrographs using the linear intercept method according to ASTM E112.

The mechanical properties of the materials were thoroughly evaluated. Vickers hardness (Hv) was measured on the polished surfaces using a microhardness tester with a load of 9.8 N (1 kgf) and a dwell time of 15 seconds, following ASTM C1327. At least ten indentations were made for each sample to ensure statistical reliability. The apparent fracture toughness ($K_{Ic}$) was estimated using the indentation fracture (IF) method from the lengths of the radial cracks emanating from the corners of the Vickers indents, calculated using the equation proposed by Anstis *et al.* [22]. Because indentation-derived $K_{Ic}$ in transformation-toughened ceramics can be influenced by local residual stresses and transformation-related crack shielding around the indent, the values reported here are used primarily for relative comparison within the present material set rather than as absolute material constants.

### *(3) Tribocorrosion-erosion test*

A custom-built slurry jet erosion-corrosion apparatus was designed and fabricated to simulate the harsh conditions of road splash. The setup consisted of a 10-liter temperature-controlled slurry reservoir equipped with a magnetic stirrer to maintain a uniform suspension of abrasive particles. A peristaltic pump circulated the slurry through a closed loop to a nozzle with a 3 mm inner diameter. Because peristaltic delivery can superimpose temporal pulsation on the mean flow, the imposed hydraulic condition is treated here as a nominal mean laboratory jet condition rather than a perfectly time-invariant impact field. The ceramic disc sample was mounted in a specialized holder that also served as a three-electrode electrochemical cell, with the sample acting as the working electrode, a platinum mesh as the counter electrode, and a saturated Ag/AgCl electrode as the reference electrode. For electrochemical testing, the exposed working area was restricted to the central jet-impinged region defined by the cell geometry; accordingly, area-normalized current densities are interpreted comparatively across identically mounted specimens.

The simulated road-splash medium was meticulously prepared for each test. The corrosive electrolyte was a 3.5 wt% NaCl solution in deionized water, a standard concentration used to simulate seawater and de-icing salt environments. The abrasive component was silica ($SiO_2$) sand with a defined particle size distribution of 200 – 300 μm [23]. The slurry was prepared with a solids concentration of 10 wt%. The test parameters were held constant for all experiments: the slurry jet was directed at the center of the sample surface at an impingement angle of 45° from a nozzle-to-sample distance of 10 mm. The apparatus was operated at a nominal mean slurry jet velocity of 10 m/s. This velocity-angle combination was selected as a controlled laboratory analogue for oblique road-splash attack on exposed suspension interfaces, where saline droplets and entrained particles strike underbody components under mixed normal and tangential loading rather than purely normal impact; in this context, 45° captures simultaneous cutting and impact components, while 10 m/s provides a moderate but repeatable impingement severity relevant to splash-driven erosion-corrosion conditions [2, 3, 26]. Direct single-particle velocimetry at the nozzle exit was not performed in the present study, so the quoted velocity should be interpreted as the nominal mean hydraulic condition rather than an independently measured particle-impact velocity. Each test was conducted at a constant temperature of 25 ± 1 °C for a total duration of 24 hours.

### *(4) Performance evaluation and post-test analysis*

The degradation of the samples was monitored with both gravimetric and electrochemical methods. The mass of each sample was measured at 4-hour intervals throughout the 24-hour test using a precision analytical balance (±0.01 mg) after careful cleaning and drying. The cumulative mass loss was converted to volume loss using the measured density of each material to provide a normalized comparison of material removal [24, 25].

Electrochemical measurements were performed using a potentiostat connected to the three-electrode cell. The Open Circuit Potential (OCP) was continuously monitored for 30 minutes before, during the entire 24-hour test, and for 30 minutes after the slurry jet was stopped to observe the processes of surface depassivation and repassivation. Potentiodynamic polarization scans were conducted from – 250 mV to + 250 mV versus OCP at a scan rate of 0.167 mV/s to determine the corrosion potential ($E_{corr}$) and corrosion current density ($i_{corr}$) both before and after the 24-hour exposure. Electrochemical Impedance Spectroscopy (EIS) was also performed at the OCP over a frequency range from 100 kHz to 10 mHz with a 10 mV AC perturbation to analyze the properties of the material-electrolyte interface [26]. Because prolonged slurry impingement may perturb the exact edge condition of the exposed zone, the absolute current-density values are interpreted cautiously, whereas relative trends among identically mounted specimens are considered more robust.

After the completion of the tests, the worn surfaces were subjected to extensive characterization. The morphology of the wear scars was examined in detail using SEM to identify the dominant material removal mechanisms. The topography and volume of the wear craters were quantified using 3D optical profilometry. To investigate the role of the toughening mechanism, XRD analysis was performed on wear-scar-centered regions to assess the stress-induced tetragonal-to-monoclinic $ZrO_2$ phase transformation. Because the finite beam footprint may partially sample adjacent unworn material, the resulting monoclinic fractions are interpreted as localized, semiquantitative measures of transformation within the damaged zone rather than perfectly crater-confined absolute values. This was compared against the XRD data from the as-sintered, unworn surfaces.

## III. Results and Discussion

### *(1) Characterization of as-sintered materials*

The physical, microstructural, and mechanical properties of the five sintered ceramic compositions are fundamental to understanding their subsequent performance under tribocorrosion-erosion conditions. The densification behavior, phase assemblage, microstructure, and baseline mechanical integrity were thoroughly evaluated and are summarized in Tables 1 and 2.

All fabricated materials achieved high relative densities exceeding 99.5 %, indicating that the selected sintering cycle of 1 550 °C for 2 hours was effective in producing nearly fully dense bodies with minimal residual porosity. This is crucial as porosity can act as a stress concentrator and initiation site for fracture, severely degrading mechanical performance. The Vickers hardness results followed a predictable trend: monolithic alumina (A100) exhibited the highest hardness (18.2 GPa), consistent with its intrinsic properties [27]. With the progressive addition of the softer 3Y-TZP phase, the hardness of the ZTA composites gradually decreased, reaching 16.7 GPa for ZTA30. Monolithic 3Y-TZP (Z100) had the lowest hardness at 13.1 GPa. Conversely, the fracture toughness showed a dramatic improvement with the incorporation of zirconia. Monolithic alumina displayed a modest toughness of 3.6 MPa·m$^{1/2}$. The addition of just 10 vol% 3Y-TZP in ZTA10 nearly doubled the toughness to 6.4 MPa·m$^{1/2}$. The toughness peaked at 8.1 MPa·m$^{1/2}$ for the ZTA20 composition, representing a 125 % increase over monolithic alumina. Further increasing the zirconia content to 30 vol% (ZTA30) resulted in a slight decrease in toughness to 7.7 MPa·m$^{1/2}$. This nonlinear behavior suggests an optimal zirconia concentration for maximizing the transformation toughening effect [18]. The Z100 sample showed a toughness of 6.1 MPa·m$^{1/2}$, superior to A100 but significantly lower than the optimized ZTA20 composite. These indentation-based $K_{Ic}$ values are therefore discussed here as comparative indicators of crack-resistance trends within a common test protocol, rather than as rigorous absolute toughness constants for transformation-toughened ceramics.

The XRD patterns of the as-sintered materials are presented in Fig. 1. The patterns confirm the expected phase compositions. The A100 pattern shows only peaks corresponding to α-$Al_2O_3$ (corundum), and the Z100 pattern is dominated by peaks of the tetragonal $ZrO_2$ phase, indicating that the 3 mol% yttria was highly effective in stabilizing this metastable phase at room temperature. The patterns for ZTA10, ZTA20, and ZTA30 show a combination of peaks from both α-$Al_2O_3$ and t-$ZrO_2$. Crucially, the intensity of peaks corresponding to the monoclinic $ZrO_2$ phase (e.g., near 28.2° and 31.5° 2θ) is negligible across all zirconia-containing samples, confirming that the processing and cooling steps did not induce premature transformation [14].

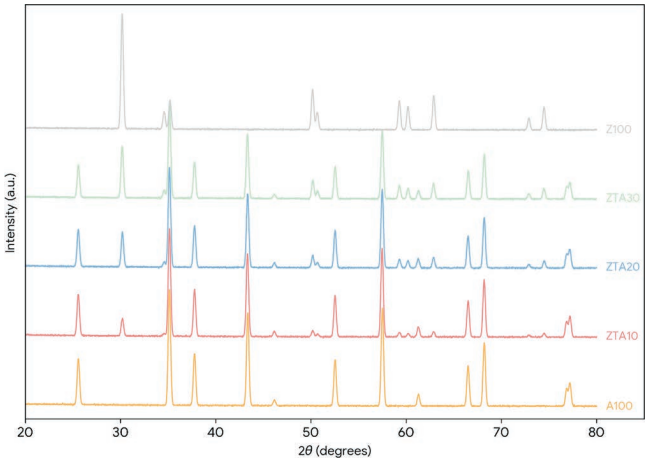



**Fig. 1:** XRD patterns of the as-sintered ceramic materials.

The quantitative phase analysis and microstructural parameters derived from XRD and SEM are detailed in Table 2. The measured phase fractions are in excellent agreement with the nominal compositions. The average grain size of the alumina matrix in the ZTA composites was observed to decrease with increasing zirconia content, from 2.2 μm in ZTA10 to 1.8 μm in ZTA30, compared to 2.5 μm in monolithic A100. This demonstrates the well-known grain growth inhibiting effect of the second-phase zirconia particles, which pin the alumina grain boundaries during sintering [28]. The zirconia grains themselves were significantly finer, with an average size of approximately 0.3 – 0.5 μm, and were found to reside primarily at the grain boundaries and triple junctions of the larger alumina grains, as well as within some larger alumina grains (intergranular and intragranular distribution).

**Table 1:** Physical and mechanical properties of as-sintered ceramic materials.

| Material ID | Composition (vol%) | Bulk Density (g/cm³) | Relative Density (%) | Vickers Hardness (GPa) | Fracture Toughness, $K_{Ic}$ (MPa·m$^{1/2}$) |
|---|---|---|---|---|---|
| A100 | 100% $Al_2O_3$ | 3.96 | 99.5 | 18.2 ± 0.4 | 3.6 ± 0.2 |
| ZTA10 | 90% $Al_2O_3$, 10% 3Y-TZP | 4.15 | 99.6 | 17.6 ± 0.3 | 6.4 ± 0.3 |
| ZTA20 | 80% $Al_2O_3$, 20% 3Y-TZP | 4.34 | 99.7 | 17.1 ± 0.3 | 8.1 ± 0.4 |
| ZTA30 | 70% $Al_2O_3$, 30% 3Y-TZP | 4.53 | 99.5 | 16.7 ± 0.4 | 7.7 ± 0.4 |
| Z100 | 100% 3Y-TZP | 6.02 | 99.8 | 13.1 ± 0.2 | 6.1 ± 0.3 |

**Table 2:** Phase composition and microstructural parameters of as-sintered materials.

| Material ID | $\alpha$-$Al_2O_3$ (vol%) | t-$ZrO_2$ (vol%) | m-$ZrO_2$ (vol%) | $Al_2O_3$ Grain Size ($\mu$m) | $ZrO_2$ Grain Size ($\mu$m) |
|---|---|---|---|---|---|
| A100 | 100 | - | - | 2.5 ± 0.6 | - |
| ZTA10 | 89.8 | 10.2 | <0.1 | 2.2 ± 0.5 | 0.3 ± 0.1 |
| ZTA20 | 80.1 | 19.9 | <0.1 | 2.0 ± 0.4 | 0.4 ± 0.1 |
| ZTA30 | 70.3 | 29.7 | <0.1 | 1.8 ± 0.4 | 0.5 ± 0.1 |
| Z100 | - | 99.9 | <0.1 | - | 0.4 ± 0.1 |

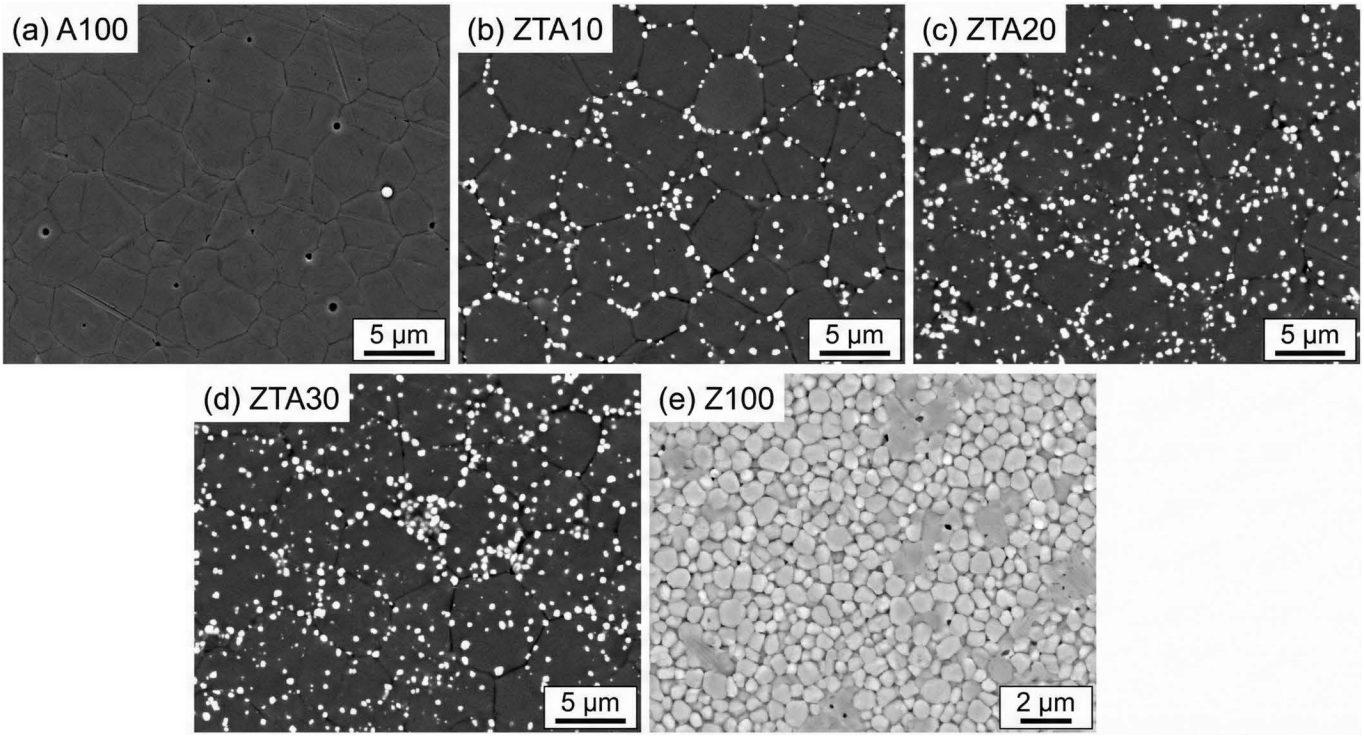



**Fig. 2:** BSE SEM micrographs of the as-sintered microstructures of (a) A100, (b) ZTA10, (c) ZTA20, (d) ZTA30, and (e) Z100.

Fig. 2 presents the backscattered electron SEM micrographs, which visually corroborate these findings. The monolithic A100 shows a dense, equiaxed grain structure. The fine-grained microstructure of monolithic Z100. The composite microstructures clearly show the bright 3Y-TZP particles (higher atomic number) homogeneously dispersed within the darker alumina matrix. The inter- and intragranular distribution of the zirconia particles is evident. This fine and uniform dispersion is essential for the effective operation of the transformation toughening mechanism, as it ensures that any propagating crack is likely to interact with the toughening phase [29]. The combination of high hardness from the continuous alumina matrix and high toughness imparted by the dispersed zirconia phase provides these ZTA composites with a balanced and superior set of initial mechanical properties compared to their monolithic constituents.

*(2) Tribocorrosion-erosion behavior: volumetric loss analysis*

The material removal due to the synergistic action of mechanical erosion by silica particles and corrosion by the 3.5 % NaCl solution was quantified by measuring the cumulative volume loss over the 24-hour test duration. The results, plotted in Fig. 3a, reveal distinct differences in the performance of the five ceramic materials. All samples exhibited an initial transient period of higher material loss, followed by a transition to a steady-state erosion rate, as indicated by the linear progression of volume loss over time.

The monolithic alumina, A100, demonstrated the poorest performance, suffering the highest total volume loss of 0.86 $mm^3$ after 24 hours. Its behavior is characteristic of a hard but brittle material under erosive attack. The impacting silica particles, although softer than alumina, possess sufficient kinetic energy to cause localized Hertzian contact stresses that exceed the fracture strength of the material, leading to the initiation and propagation of microcracks [30]. The dominant material removal mechanism is brittle fracture, involving lateral and radial cracking, which results in the detachment of entire grains or large fragments (grain pull-out), leading to a high rate of volume loss [31].

In contrast, monolithic zirconia, Z100, showed significantly better resistance, with a total volume loss of 0.41 $mm^3$, less than half that of A100. Despite its lower

hardness, Z100's substantially higher fracture toughness allows it to absorb more impact energy through plastic deformation and stress-induced phase transformation before fracture occurs [32]. This reduces the extent of cracking and shifts the material removal mechanism towards a more ductile mode involving ploughing and cutting, resulting in a lower material removal rate [33, 34].

The ZTA composites exhibited superior performance compared to both monolithic constituents. The volume loss for ZTA10, ZTA20, and ZTA30 was 0.22 $mm^3$, 0.15 $mm^3$, and 0.29 $mm^3$, respectively. Notably, the ZTA20 composition displayed the lowest volume loss, achieving a nearly six-fold improvement in resistance compared to monolithic alumina and a 2.7-fold improvement over monolithic zirconia. This highlights the powerful synergistic effect of combining the two phases. The hard alumina matrix provides the primary resistance to indentation and abrasion from the slurry particles, while the finely dispersed zirconia particles act as a crucial defense against crack propagation. When a microcrack is initiated in the alumina matrix by an impact, its propagation is impeded as it encounters the high-stress compressive field generated by the t→m transformation of a nearby zirconia particle [35]. This mechanism effectively dissipates the impact energy, arrests crack growth, and prevents the large-scale brittle fracture observed in A100.

The steady-state erosion rates, calculated from the linear portion of the curves in Fig. 3a, are presented in the bar chart in Fig. 3b and summarized in Table 3. The trend mirrors the total volume loss, with ZTA20 exhibiting the lowest steady-state erosion rate of 5.9 x $10^{-3}$ $mm^3/h$. The performance ranking is clear: ZTA20 > ZTA10 > ZTA30 > Z100 > A100. The fact that ZTA20 outperforms ZTA30 suggests that there is an optimal zirconia content. While increasing zirconia content enhances toughness, it simultaneously reduces hardness. The superior performance of ZTA20 indicates that it strikes the ideal balance between hardness (resisting initial particle penetration) and toughness (resisting subsequent crack propagation) for the specific conditions of this tribocorrosion-erosion test [36].

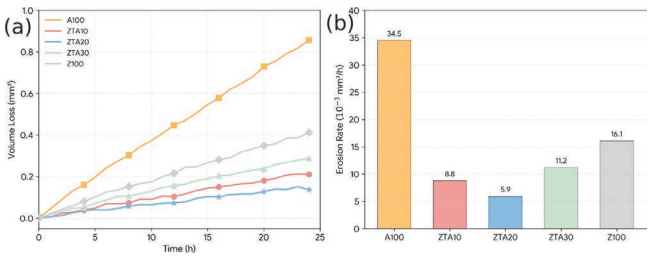



**Fig. 3:** (a) Cumulative volume loss as a function of time for all five ceramic materials under slurry jet tribocorrosion-erosion testing. (b) Steady-state erosion rates calculated from the linear region of the volume loss curves. .

**Table 3:** Steady-state erosion rate and post-test surface roughness.

| Material ID | Steady-State Erosion Rate ($10^{-3}$ $mm^3/h$) | Average Roughness (*Ra*) of Wear Scar (μm) |
|---|---|---|
| A100 | 34.5 | 1.85 |
| ZTA10 | 8.8 | 0.62 |
| ZTA20 | 5.9 | 0.45 |
| ZTA30 | 11.2 | 0.78 |
| Z100 | 16.1 | 0.95 |

### *(3) Analysis of electrochemical behavior*

While ceramics are generally considered corrosion-resistant, the continuous mechanical damage from particle impingement can alter their surface chemistry and electrochemical response. Fig. 4 displays the evolution of the Open Circuit Potential (OCP) for each material before, during, and after the slurry jet impingement. Before the test (t < 0), all samples exhibited a stable OCP, indicative of a passive surface in the NaCl solution. Upon initiation of the slurry jet (at t = 0), a sharp and immediate drop in OCP was observed for all materials. This negative shift signifies a transition to a more active surface state, caused by the mechanical removal of any pre-existing passive layers and the generation of a fresh, damaged surface with high-density defects like microcracks and strained bonds, which are more electrochemically active [37]. Throughout the 24-hour test, the OCP remained at this lower, fluctuating potential. These oscillations are attributed to repeated depassivation and partial repassivation under particle impingement, with a likely additional contribution from flow pulsation associated with peristaltic pumping [38, 39]. Accordingly, the OCP fluctuations are interpreted qualitatively as indicators of dynamic surface activation rather than as a purely stochastic signature of single-particle impacts. After the slurry jet was stopped (t > 24 h), the OCP began to slowly drift back towards more positive values, indicating a gradual repassivation or stabilization of the damaged surface. The magnitude of the initial OCP drop was most pronounced for A100, followed by Z100, and was least significant for the ZTA composites, particularly ZTA20. This suggests that the ZTA20 surface is more resilient to mechanical depassivation, aligning with its superior material loss performance.

The potentiodynamic polarization curves, shown in Fig. 5, provide quantitative insights into the corrosion behavior. Before erosion (Fig. 5a), all materials displayed very low corrosion current densities ($i_{corr}$), characteristic of highly passive materials. After 24 hours of tribocorrosion-erosion (Fig. 5b), the polarization curves for all samples shifted towards higher current densities, confirming that the mechanical damage increased their electrochemical activity. The extracted corrosion parameters are listed in Table 4. While the absolute $i_{corr}$ values remain low compared to metals, the relative changes are significant. A100 showed the largest increase in $i_{corr}$,

consistent with its extensive surface damage. The ZTA composites, especially ZTA20, maintained the lowest $i_{corr}$ values after the test, indicating a greater ability to resist electrochemical degradation even in a mechanically damaged state.

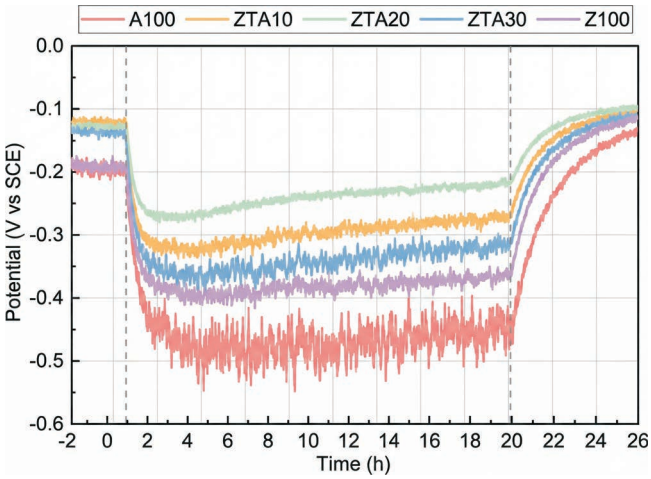



**Fig. 4:** OCP evolution versus time for the ceramic samples in 3.5 % NaCl slurry.

Further analysis was conducted using Electrochemical Impedance Spectroscopy (EIS). The Nyquist plots in Fig. 6 show the impedance response before and after the test. Before testing (Fig. 6a), all materials exhibit very large, semi-circular arcs, indicative of a high apparent polarization resistance and a highly capacitive surface. For ceramic-electrolyte interfaces, however, the semicircle diameter can reflect combined contributions from interfacial charge transfer, defect or pore pathways, and non-ideal capacitive behavior; therefore it is discussed here as an overall interfacial impedance response rather than as a rigorously isolated charge-transfer resistance [40]. After 24 hours of tribocorrosion-erosion (Fig. 6b), the diameters of the semicircles for all materials decreased dramatically, signifying a substantial reduction in apparent polarization resistance. This confirms that the erosion damage severely compromised the protective nature of the ceramic surfaces, creating easier pathways for interfacial electrochemical reactions. Consistent with all other data, the post-test Nyquist plot for ZTA20 retained the largest diameter, confirming it maintained the most corrosion-resistant surface among the tested materials. The electrochemical results, while secondary to the massive material loss from mechanical erosion, consistently support the performance ranking derived from the volume loss data and demonstrate that the ZTA composites, particularly ZTA20, possess a superior ability to withstand the coupled chemical-mechanical attack.

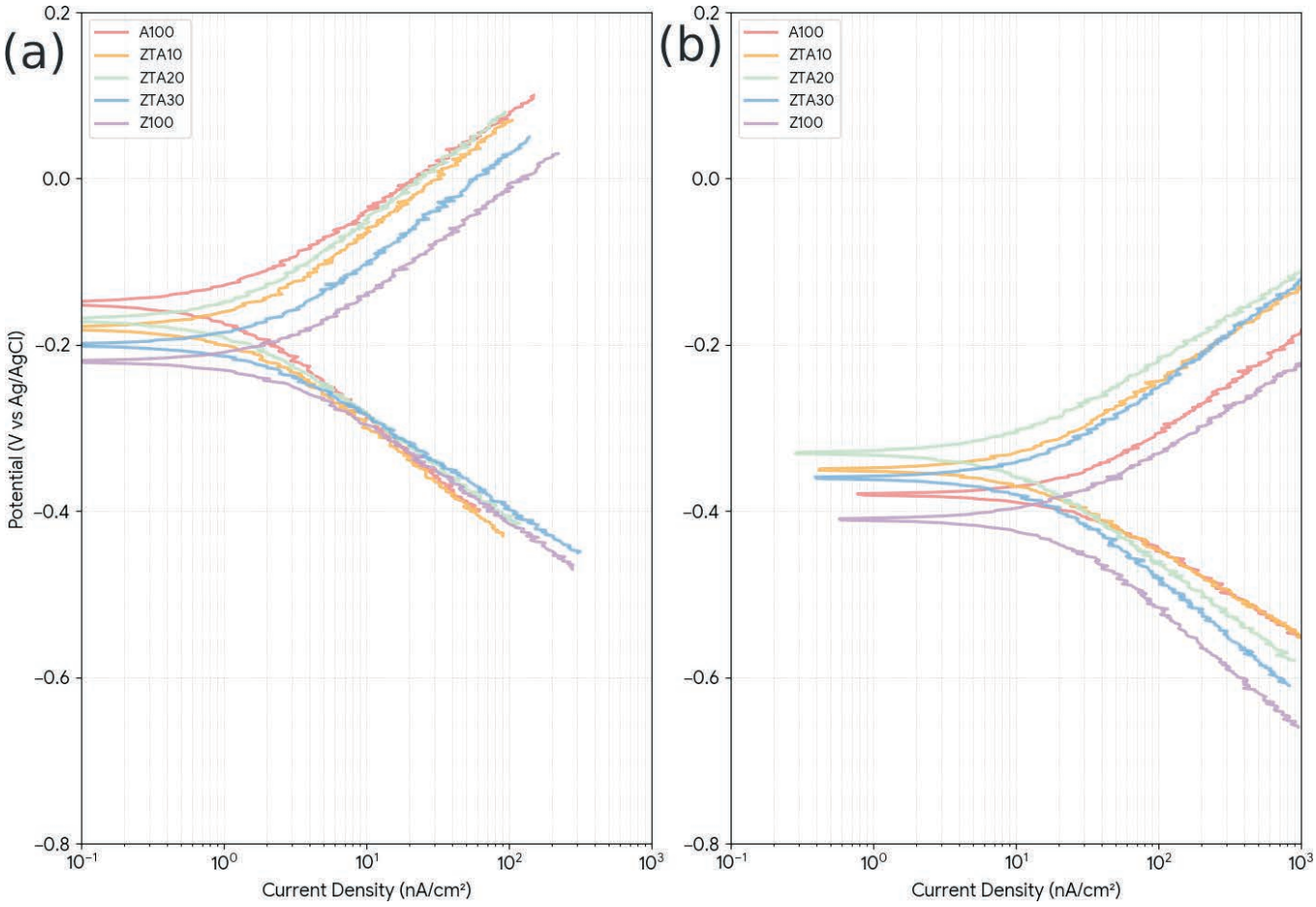



**Fig. 5:** Potentiodynamic polarization curves for the ceramic materials in 3.5 % NaCl solution (a) before and (b) after 24 hours of tribocorrosion-erosion testing.

**Table 4:** Electrochemical parameters derived from potentiodynamic polarization.

| Material ID | E_corr (V vs Ag/AgCl) - Before Test | i_corr (nA/cm²) - Before Test | E_corr (V vs Ag/AgCl) - After Test | i_corr (nA/cm²) - After Test |
|---|---|---|---|---|
| A100 | -0.15 | 1.2 | -0.38 | 25.6 |
| ZTA10 | -0.18 | 1.5 | -0.35 | 11.4 |
| ZTA20 | -0.17 | 1.3 | -0.33 | 8.9 |
| ZTA30 | -0.20 | 1.8 | -0.36 | 14.5 |
| Z100 | -0.22 | 2.5 | -0.41 | 19.8 |

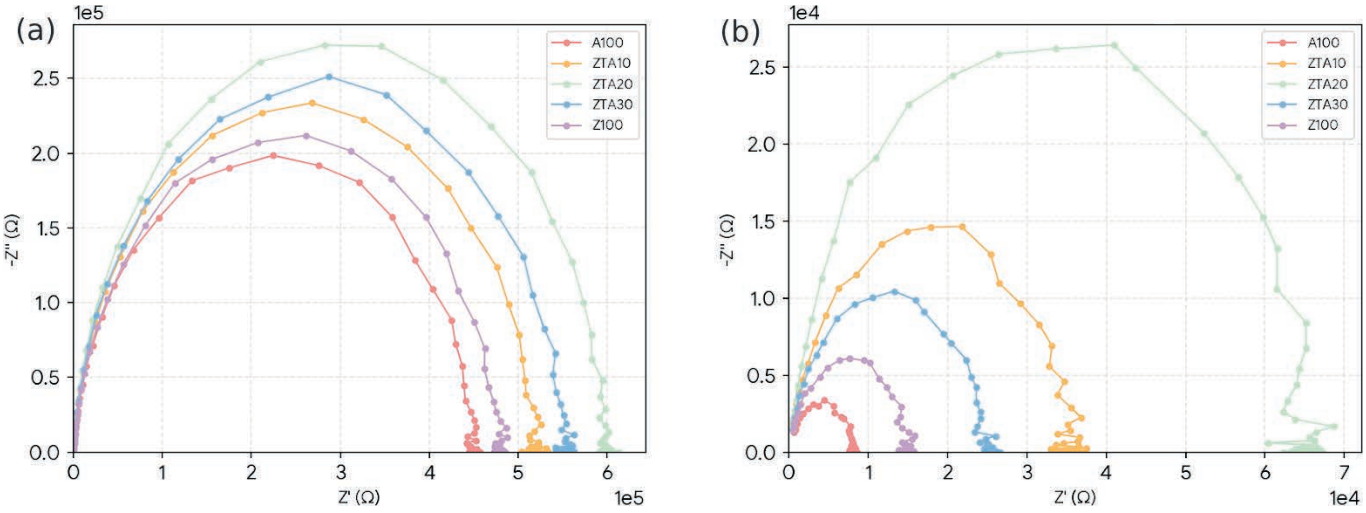



**Fig. 6:** Nyquist plots from EIS measurements for all materials (a) before and (b) after 24 hours of tribocorrosion-erosion testing.

### *(4) Analysis of surface degradation mechanisms*

To elucidate the physical mechanisms responsible for the observed differences in performance, the wear scars were meticulously examined using SEM and 3D profilometry. The SEM micrographs in Fig. 7 provide compelling visual evidence of the distinct degradation modes for each material. The surface of A100 is characterized by extensive brittle fracture. Widespread intergranular cracking is visible, and numerous locations show evidence of entire grains having been dislodged (grain pull-out), leaving deep cavities. This mode of material removal is inefficient in terms of energy absorption and leads to rapid surface degradation and the high volume loss observed.

The wear scar on Z100 presents a different morphology. While some micro-cracking is present, the surface also exhibits shallow ploughing grooves and microcutting features created by the scraping action of the silica particles. This behavior is consistent not only with the higher toughness of zirconia, but also with the relatively small hardness contrast between Z100 (13.1 GPa) and silica erodent particles (typically about 10 – 12 GPa), a regime in which brittle-material erosion is less dominated by catastrophic lateral cracking and more influenced by mixed ploughing and crushing processes [36, 41]. Consequently, Z100 can absorb a larger fraction of impact energy before fragment detachment occurs, resulting in lower material loss than alumina.

The ZTA composites display a hybrid degradation mechanism that leverages the strengths of both constituents. The wear scar on the best-performing ZTA20 sample is remarkably smoother than that of A100. While some ploughing is visible on the alumina grains, the most significant feature is the absence of large-scale grain pull-out. High-magnification images reveal microcracks that have been arrested or deflected upon intersecting with the zirconia particles. This crack interaction is the macroscopic manifestation of the transformation toughening mechanism at work, preventing small-scale damage from coalescing into catastrophic material removal [45]. The degradation appears to be a more controlled, layer-by-layer removal process rather than the wholesale ejection of material seen in A100. The surfaces of ZTA10 and ZTA30 show slightly more damage than ZTA20, consistent with their intermediate volume loss performance.

The 3D optical profilometry images in Fig. 8 provide a quantitative, macroscopic view of the wear scars. The images visually confirm the severity of material loss, with the A100 sample exhibiting the deepest and widest wear crater. The ZTA20 crater is clearly the most shallow and narrow, corroborating the gravimetric data. The surface roughness (*Ra*) within the wear scar was also measured (Table 4). The heavily damaged A100 surface was the roughest (1.85 µm), while the ZTA20 surface was the smoothest (0.45 µm). The smoother surface of ZTA20 is advantageous as it presents fewer stress-concentrating features for subsequent particle impacts, contributing to its lower steady-state erosion rate.

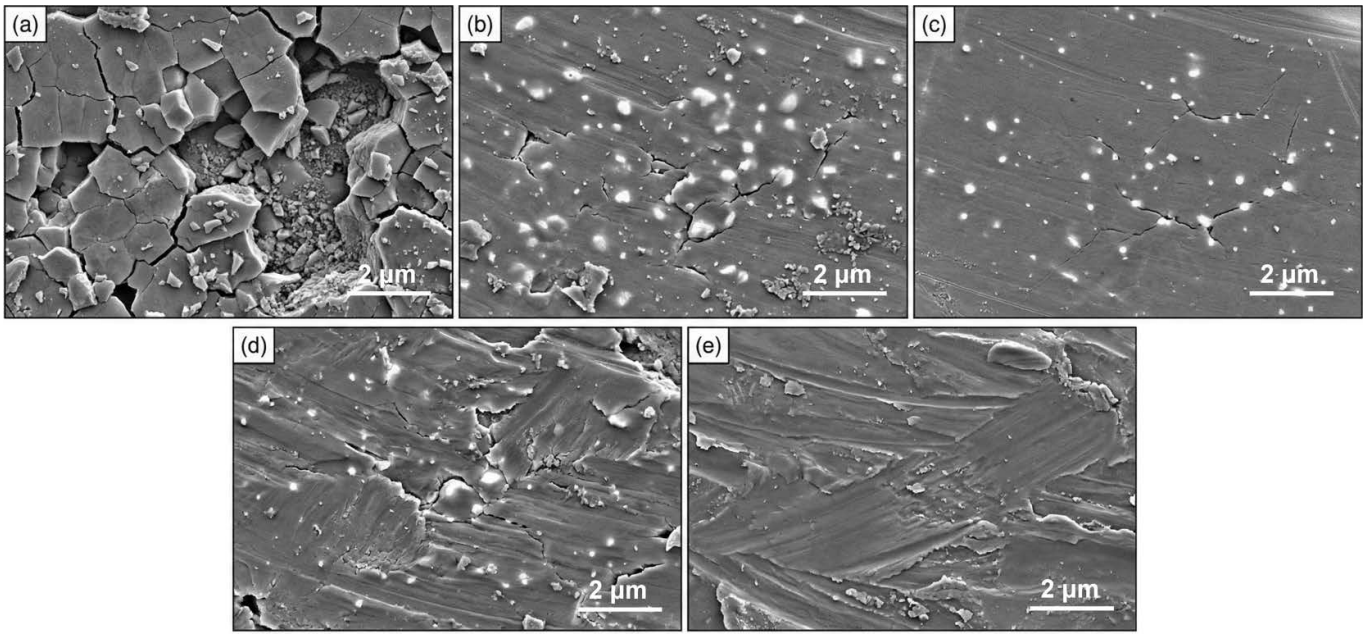



**Fig. 7:** SEM micrographs of (a) A100, (b) ZTA10, (c) ZTA20, (d) ZTA30, (e) Z100 after 24 hours of tribocorrosion-erosion testing.

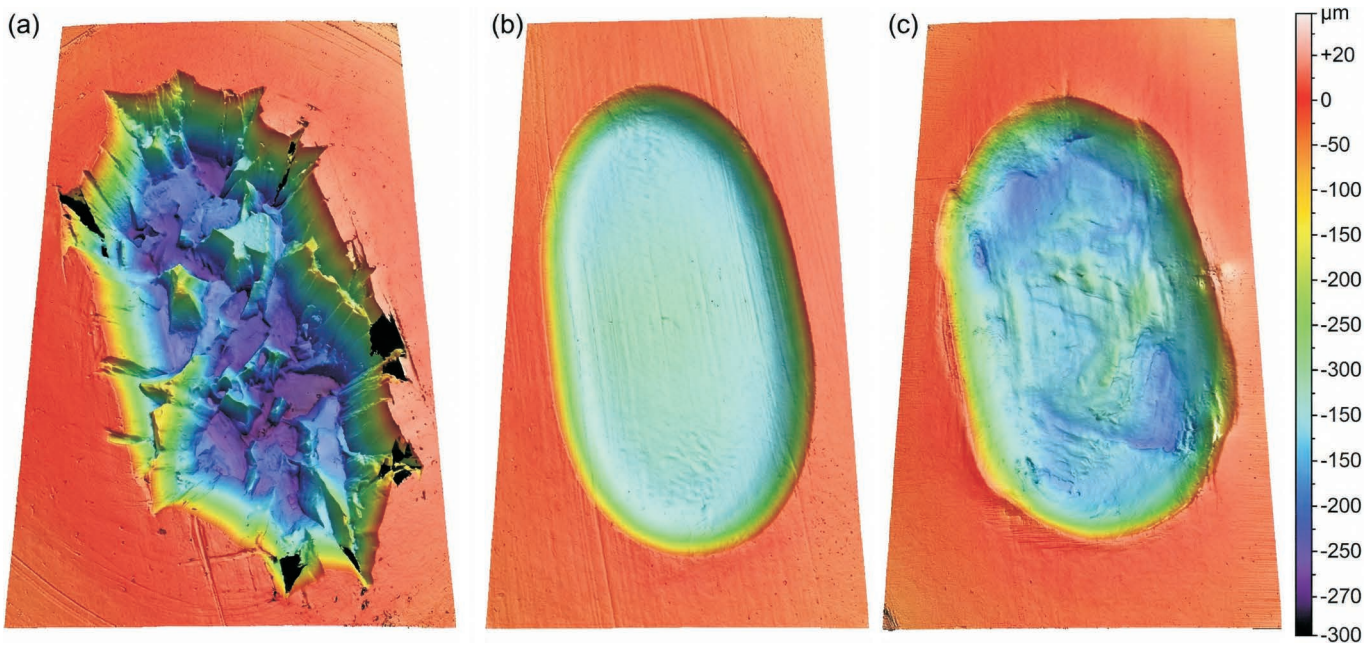



**Fig. 8:** 3D optical profilometry images of the wear craters on the surfaces of (a) A100, (b) ZTA20, and (c) Z100 after 24 hours of testing.

The definitive evidence of the active toughening mechanism is provided by the XRD analysis of the wear scars, shown in Fig. 9. Compared to the as-sintered patterns, the XRD patterns from the worn surfaces of Z100, ZTA10, ZTA20, and ZTA30 show the distinct emergence and growth of peaks corresponding to the monoclinic zirconia (m- $ZrO_2$) phase. This is direct evidence of the stress-induced martensitic transformation from t-$ZrO_2$ to m-$ZrO_2$ occurring in response to the high stresses generated by the particle impacts [46]. Quantitative Rietveld analysis, centered on the wear-scar region, indicated that the monoclinic phase fraction within the damaged zone of the ZTA20 sample increased from < 0.1 % to approximately 45 %. The ZTA10 and ZTA30 samples showed corresponding localized transformed fractions of about 38 % and 42 %, respectively, while the Z100 sample reached about 55 %. Because the finite X-ray footprint can partly average the crater with adjacent unworn surface, these values should be interpreted as semiquantitative wear-zone estimates rather than perfectly crater-confined absolute phase fractions. The substantial transformation in the ZTA samples confirms that this energy-dissipating mechanism was highly active and is the primary reason for their enhanced toughness and superior erosion resistance. The fact that Z100 transformed more but performed worse than the ZTA composites suggests that the toughening mechanism alone is not sufficient; it must be paired with the high hardness of the alumina matrix to achieve optimal performance against abrasive and erosive wear.

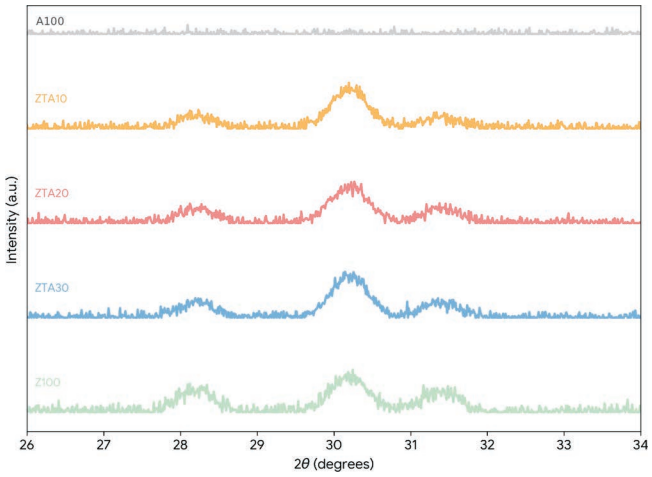



**Fig. 9:** XRD patterns taken from within the wear scars after 24 hours of tribocorrosion-erosion testing.

## IV. Conclusions

This comprehensive investigation successfully evaluated the performance of Zirconia-Toughened Alumina (ZTA) composites as a potential material for automotive suspension insert washers operating under severe tribo-corrosion-erosion conditions. A simulated road-splash environment, consisting of a 3.5 % NaCl slurry with 200 – 300 µm silica sand abrasives, was used to assess the material degradation in a slurry jet impingement test.

The key findings of this study can be summarized as follows:

1. High-density (> 99.5 %) ZTA composites with 10, 20, and 30 vol% 3Y-TZP were successfully fabricated. The incorporation of zirconia significantly enhanced the fracture toughness, with the ZTA20 composition achieving a peak toughness of 8.1 MPa·m$^{1/2}$, a 125 % improvement over monolithic alumina.
2. Under coupled tribocorrosion-erosion conditions, the ZTA composites demonstrated vastly superior resistance to material loss compared to both monolithic alumina (A100) and monolithic yttria-stabilized zirconia (Z100). The ZTA20 composition exhibited the best performance, with a steady-state erosion rate nearly six times lower than that of alumina.
3. The superior performance of ZTA is attributed to a synergistic combination of high hardness provided by the alumina matrix and high fracture toughness imparted by the zirconia dispersoids. Post-test analysis confirmed that the primary degradation mechanism in alumina was brittle fracture and grain pull-out, whereas the ZTA composites resisted material removal through the activation of stress-induced tetragonal-to-monoclinic phase transformation in the zirconia phase. This energy-dissipating mechanism was directly verified by XRD analysis of the wear scars, which showed a significant increase in the monoclinic phase fraction.
4. Electrochemical measurements indicated that while all ceramics are inherently corrosion-resistant, the mechanical damage from erosion significantly increases surface electrochemical activity. The ZTA composites, particularly ZTA20, maintained a more electrochemically stable and resistant surface compared to the monolithic ceramics after prolonged exposure.

In conclusion, Zirconia-Toughened Alumina, specifically the composition with 20 vol% zirconia, has been identified as an exceptionally promising material for suspension components. Its unique ability to combine hardness with toughness through the transformation toughening mechanism provides outstanding resilience in harsh environments where coupled mechanical wear and corrosion are prevalent. The results of this study provide a strong basis for the adoption of ZTA ceramics to enhance the durability, reliability, and lifespan of critical automotive components. Future work should focus on long-term field trials and the investigation of performance under a wider range of temperatures and abrasive conditions.

## Acknowledgements

This work has been supported by the Science and Technology Research Program of Chongqing Municipal Education Commission (Grant No. KJZD-K202503202).

## References

1 Akin, I.: Investigation of the microstructure, mechanical properties and cell viability of zirconia-toughened alumina composites reinforced with carbon nanotubes, *J. Ceram. Soc. Jpn.*, **123**, 405 – 413, (2015).

2 Putra, T.E., Husaini, Ikbal, M.: Automotive suspension component behaviors driven on flat and rough road surfaces, *Heliyon*, **7**, e07528, (2021).

3 Lim, H., Lee, S., Lee, S., Kim, C.: Corrosion analysis of vehicle materials and feasibility assessment of magnesium alloys under deicing agent exposure, *Corros. Eng. Sci. Technol.*, **60**, 1478422X251376903, (2025).

4 Mathew, M.T., Cheng, K.Y., Sun, Y., Barao, V.A.R.: The progress in tribocorrosion research (2010 – 2021): focused on orthopedics and dental implants, *J. Bio Tribocorros.*, **9**, 48, (2023).

5 Gafur, M.A., Al-Amin, M., Sarker, M.S.R., Alam, M.Z.: Structural and mechanical properties of alumina-zirconia (ZTA) composites with unstabilized zirconia modulation, *Mater. Sci. Appl.*, **12**, 542 – 560, (2021).

6 Lopes, A.C.O., Coelho, P.G., Witek, L., Benalcázar Jalkh, E.B., Gênova, L.A., Monteiro, K.N., *et al.*: Nanomechanical and microstructural characterization of a zirconia-toughened alumina composite after aging, *Ceram. Int.*, **45**, 8840 – 8846, (2019).

7 Murray, J.W., Leva, A., Joshi, S., Hussain, T.: Microstructure and wear behaviour of powder and suspension hybrid $Al_2O_3$-YSZ coatings, *Ceram. Int.*, **44**, 8498 – 8504, (2018).

8 Naglieri, V., Palmero, P., Montanaro, L., Chevalier, J.: Elaboration of alumina-zirconia composites: role of the zirconia content on the microstructure and mechanical properties, *Materials*, **6**, 2090 – 2102, (2013).

9 Teow, H.L., Sivanesan, S., Noum, S.Y.E., Soosai, A., Muniandy, S.: Effect of graphene oxide addition on the microstructure and mechanical properties of two-stage sintered zirconia-toughened alumina composites, *MATEC Web Conf.*, **335**, 03019, (2021).

10 Fujii, T., Tohgo, K., Putra, P.B., Shimamura, Y.: Fabrication of alumina-PSZ composites via spark plasma sintering and their mechanical properties, *J. Mech. Behav. Biomed. Mater.*, **91**, 45 – 53, (2019).

[11] Wu, T., Su, J., Li, Y., Zhao, H., Zhang, Y., Zhang, M., *et al.*: Wear resistance mechanism of alumina ceramics containing $Gd_2O_3$, *Materials*, **11**, 2054, (2018).

[12] Hannink, R.H.J., Kelly, P.M., Muddle, B.C.: Transformation toughening in zirconia-containing ceramics, *J. Am. Ceram. Soc.*, **83**, 461 – 487, (2000).

[13] Boniecki, M., Sadowski, T., Gołębiewski, P., Węglarz, H., Piątkowska, A., Romaniec, M., *et al.*: Mechanical properties of alumina/zirconia composites, *Ceram. Int.*, **46**, 1033 – 1039, (2020).

[14] Abbas, S., Maleksaeedi, S., Kolos, E., Ruys, A.J.: Processing and properties of zirconia-toughened alumina prepared by gelcasting, *Materials*, **8**, 4344 – 4362, (2015).

[15] Mamivand, M., Asle Zaeem, M., El Kadiri, H.: Phase field modeling of stress-induced tetragonal-to-monoclinic transformation in zirconia and its effect on transformation toughening, *Acta Mater.*, **64**, 208 – 219, (2014).

[16] Bartolomé, J.F., Gutiérrez-González, C.F., Pecharromán, C., Moya, J.S.: Synergistic toughening mechanism in 3Y-TZP/Nb composites, *Acta Mater.*, **55**, 5924 – 5933, (2007).

[17] Varga, M., Grundtner, R., Maj, M., Tatzgern, F., Alessio, K.O.: Impact-abrasive wear resistance of high alumina ceramics and zirconia-toughened alumina, *Wear*, **522**, 204700, (2023).

[18] Tang, D., Lim, H.B., Lee, K.J., Lee, C.H., Cho, W.S.: Evaluation of mechanical reliability of zirconia-toughened alumina composites for dental implants, *Ceram. Int.*, **38**, 2429 – 2436, (2012).

[19] Herrmann, M., Seipel, B., Schilm, J., Nickel, K.G., Michael, G., Krell, A.: Hydrothermal corrosion of zirconia-toughened alumina at 200 °C, *J. Eur. Ceram. Soc.*, **25**, 1805 – 1812, (2005).

[20] Pasaribu, H.R., Reuver, K.M., Schipper, D.J., Ran, S., Wiratha, K.W., Winnubst, A.J.A., *et al.*: Environmental effects on friction and wear of dry sliding zirconia and alumina ceramics doped with copper oxide, *Int. J. Refract. Met. Hard Mater.*, **23**, 386 – 390, (2005).

[21] Zygmuntowicz, J., Żurowski, R., Tomaszewska, J., Wachowski, M., Torzewski, J., Piotrkiewicz, P., *et al.*: $Al_2O_3/ZrO_2$ materials as an environmentally friendly solution for linear infrastructure applications, *Materials*, **14**, 2375, (2021).

[22] Anstis, G.R., Chantikul, P., Lawn, B.R., Marshall, D.B.: A critical evaluation of indentation techniques for measuring fracture toughness: I, direct crack measurements, *J. Am. Ceram. Soc.*, **64**, 533 – 538, (1981).

[23] López, D.M., Alonso Falleiros, N., Tschiptschin, A.P.: Use of electrochemical tests for assessment of the effect of erosive particle size on the erosion-corrosion behaviour of AISI 304L austenitic stainless steel, *Mater. Res.*, **19**, 451 – 458, (2016).

[24] Brownlie, F., Hodgkiess, T., Pearson, A., Galloway, A.M.: A study on the erosion-corrosion behaviour of engineering materials used in the geothermal industry, *Wear*, **477**, 203821, (2021).

[25] Oka, Y.I., Yoshida, T.: Practical estimation of erosion damage caused by solid particle impact: part 2, mechanical properties of materials directly associated with erosion damage, *Wear*, **259**, 102 – 109, (2005).

[26] Zhao, J., Feng, Y., Gao, H., Wang, L., Yang, X., Gu, Y.: Erosion-corrosion behavior of friction stud welded joints of X65 pipelines in simulated seawater under different flow rates, *Materials*, **16**, 4326, (2023).

[27] Savio, S., Singh, S., Ramakrishna, B., Vanitha, C.: Sintering of alumina using a modified two-step sintering process, *Adv. Appl. Ceram.*, **124**, 123 – 128, (2025).

[28] Keller, S., Osswald, B., Kern, F.: Properties of alumina-10 vol% zirconia composites: the role of alumina starting powders, *Open Ceram.*, **24**, 100875, (2025).

[29] Ritter, J.E., Buckman, K.J., Jakus, K., Rosenfeld, L., Strzepa, P.: Erosion damage in glass and alumina, *J. Am. Ceram. Soc.*, **67**, 11 – 18, (1984).

[30] Busca, G.: Silica-alumina catalytic materials: A critical review, *Catal. Today*, **357**, 621 – 629, (2020).

[31] Gremillard, L., Cardenas, L., Reveron, H., Douillard, T., Vogl, A., Hans, K., *et al.*: Microstructure and hydrothermal ageing of alumina-zirconia composites modified by laser engraving, *J. Eur. Ceram. Soc.*, **40**, 2077 – 2089, (2020).

[32] Stawarczyk, B., Frevert, K., Ender, A., Roos, M., Sener, B., Wimmer, T.: Comparison of four monolithic zirconia materials with conventional ones: contrast ratio, grain size, four-point flexural strength and two-body wear, *J. Mech. Behav. Biomed. Mater.*, **59**, 128 – 138, (2016).

[33] Arellano Moncayo, A.M., Peñate, L., Arregui, M., Giner-Tarrida, L., Cedeño, R.: State of the art of different zirconia materials and their indications according to evidence-based clinical performance, *Dent. J.*, **11**, 18, (2023).

[34] Almohammed, S.N., Alshorman, B., Abu-Naba'a, L.A.: Mechanical properties of five esthetic ceramic materials used for monolithic restorations: A comparative in vitro study, *Ceramics*, **6**, 1031 – 1049, (2023).

[35] Tsukamoto, H.: Enhancement of transformation toughening of partially stabilized zirconia by some additives, *Ceram. Int.*, **48**, 20675 – 20689, (2022).

[36] Lathabai, S., Pender, D.C.: Microstructural influence in slurry erosion of ceramics, *Wear*, **189**, 122 – 135, (1995).

[37] Li, L., Wang, Z., He, S., Zheng, Y.: Correlation between depassivation and repassivation processes determined by single particle impingement and its role in critical flow velocity for erosion-corrosion, *J. Mater. Sci. Technol.*, **89**, 158 – 166, (2021).

[38] Formato, G., Romano, R., Formato, A., Sorvari, J., Koiranen, T., Pellegrino, A., Villecco, F.: Fluid-structure interaction modeling applied to peristaltic pump flow simulations, *Machines*, **7**, 50, (2019).

[39] Manopoulos, C., Tsoukalis, A., Mathioulakis, D.: Suppression of flow pulsations and energy consumption of a drug delivery roller pump based on a novel tube design, *Proc. Inst. Mech. Eng. C*, **236**, 7587 – 7603, (2022).

[40] Liu, C., Bi, Q., Leyland, A., Matthews, A.: An electrochemical impedance spectroscopy study of the corrosion behaviour of PVD coated steels in 0.5 N NaCl aqueous solution: part I. establishment of equivalent circuits for EIS data modelling, *Corros. Sci.*, **45**, 1243 – 1256, (2003).

[41] Shipway, P. H., Hutchings, I. M.: The role of particle properties in the erosion of brittle materials, *Wear*, **193**, 105 – 113, (1996).

[42] Sutar, H., Mishra, S.C., Sahoo, S.K., Satapathy, A., Kumar, V.: Morphology and solid particle erosion wear behavior of red mud composite coatings, *Nat. Sci.*, **4**, 832 – 838, (2012).

[43] Aumelas, V., Maj, G., Calvé, P.L., Smith, M., Gambiez, B., Mourrat, X.: A new methodology for hydro-abrasive erosion tests simulating penstock erosive flow, *IOP Conf. Ser. Earth Environ. Sci.*, **49**, 122012, (2016).

[44] Stack, M.M., Abdulrahman, G.H.: Mapping erosion-corrosion of carbon steel in oil exploration conditions: characterizing mechanisms and synergies, *Tribol. Int.*, **43**, 1268 – 1277, (2010).

[45] Chevalier, J., Olagnon, C., Fantozzi, G.: Crack propagation and fatigue in zirconia-based composites, *Compos. Part A*, **30**, 525 – 530, (1999).

[46] Mochales, C., Maerten, A., Rack, A., Cloetens, P., Mueller, W.D., Zaslansky, P., *et al.*: Monoclinic phase transformations of zirconia-based dental prostheses induced by clinically practised surface manipulations, *Acta Biomater.*, **7**, 2994 – 3002, (2011).